

Optimally accurate thermal-wave cavity photopyroelectric measurements of pressure-dependent thermophysical properties of air: Theory and experiments

Chi-Hang Kwan, Anna Matvienko, and Andreas Mandelis^{a)}

Center for Advanced Diffusion-Wave Technologies, Department of Mechanical and Industrial Engineering, University of Toronto, Toronto M5S3G8, Canada

(Received 26 June 2007; accepted 10 September 2007; published online 5 October 2007)

An experimental technique for the measurement of thermal properties of air at low pressures using a photopyroelectric (PPE) thermal-wave cavity (TWC) was developed. In addition, two theoretical approaches, a conventional one-dimensional thermal-wave model and a three-dimensional theory based on the Hankel integral, were applied to interpret the thermal-wave field in the thermal-wave cavity. The importance of radiation heat transfer mechanisms in a TWC was also investigated. Radiation components were added to the purely conductive model by linearizing the radiation heat transfer component at the cavity boundary. The experimental results indicate that the three-dimensional model is necessary to describe the PPE signal, especially at low frequencies where thermal diffusion length is large and sideways propagation of the thermal-wave field becomes significant. Radiation is found to be the dominant contributor of the PPE signal at high frequencies and large cavity lengths, where heat conduction across the TWC length is relatively weak. The three-dimensional theory and the Downhill Simplex algorithm were used to fit the experimental data and extract the thermal diffusivity of air and the heat transfer coefficient in a wide range of pressures from 760 to 2.6 Torr. It was shown that judicious adjustments of cavity length and computational best fits to frequency-scanned data using three-dimensional photopyroelectric theory lead to optimally accurate value measurements of thermal diffusivity and heat transfer coefficient at various pressures. © 2007 American Institute of Physics. [DOI: 10.1063/1.2793503]

I. INTRODUCTION

During the past two decades, photothermal techniques have been extensively employed for the determination of thermophysical properties of materials. These techniques usually apply a modulated laser beam as the heat source to induce a periodical temperature fluctuation (thermal-wave field) in a sample. By measuring the amplitude and phase lag of the thermal-wave signal a distance away from the heat source and solving the thermal diffusion equations associated with the heat transfer mechanisms, the thermal properties of the investigated medium can be evaluated. The first photothermal experimental device designed to measure heat propagation for liquids and gases, named the thermal-wave cavity (TWC), was introduced in 1995.¹ In its original configuration, a modulated laser impinging on a thin metallic film was used as a thermal-wave generator (TWG). The induced temperature oscillations then propagate through the intracavity medium onto a pyroelectric sensor at the opposing side. The pyroelectric sensor (usually polyvinylidene fluoride film, PVDF) converts the thermal waves into a voltage signal, which can be measured and recorded by a lock-in amplifier. This configuration has been widely used to measure thermal diffusivity of gases¹⁻⁵ and liquids.⁶⁻¹⁰ Several other versions of the original configuration were then introduced in litera-

ture. A modification to the classical configuration is the inverse photopyroelectric technique.¹¹⁻¹⁷ In this method, the temperature fluctuation is introduced to the back side of the pyroelectric sensor.^{14,16,17} The advantage of this setup is that the thermal properties of the sample can be determined with very good precision due to the small dc temperature difference across the sample layer. Another variation of the TWC is a photopyroelectric interferometry setup.¹⁸ In this configuration, two laser beams are incident on opposite sides of a PVDF detector after each beam passes through a transparent wall (one as the sample and the other as the reference). The purpose of this design is to obtain simultaneous measurements of both thermal and optical properties of the sample material.

To our best knowledge, the foregoing applications of the TWC measurement techniques have all adopted a one-dimensional thermal-wave theory to describe the detected signal. Although this assumption greatly simplifies the theoretical model, a one-dimensional approach may not be adequate to describe the experimental results, if the laser beam spot size is sufficiently small compared to the cavity diameter, or the cavity length is large compared to the thermal diffusion length.

The first attempt to address the dimensionality issue was published by our group recently.¹⁹ In that study, the four layers of the TWC were studied and attention was paid to the circumferential boundary conditions in order to calculate the theoretical three-dimensional signal by means of eigenfunc-

^{a)} Author to whom correspondence should be addressed. Electronic mail: mandelis@mie.utoronto.ca

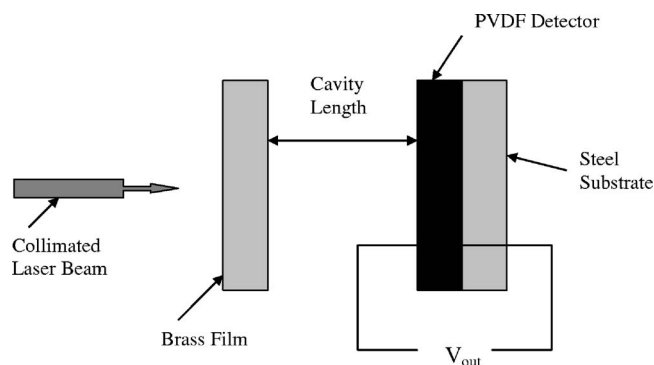


FIG. 1. Experimental setup.

tions of the heat diffusion equation in cylindrical coordinates. Although this method is highly realistic, it also renders the mathematics very cumbersome. In the present study, we introduced an alternative method to determine the lateral contributions of the thermal-wave field to the photopyroelectric signal of a TWC through the use of the Hankel integral.²⁰ The three-dimensional theoretical signals obtained by this method are used to interpret the experimental results under different hypobaric pressures and cavity lengths. The limits of validity of the conventional one-dimensional models are also explored.

The thermal properties of air at low pressures are poorly described in the literature. To our best knowledge, there are few reports presenting the measured values of thermal conductivity of air at low pressures. The most recent of those were published more than half a century ago.^{21–24} Even fewer papers have been published on the thermal diffusivity measurements at low pressures.³

In this study, we applied the thermal-wave cavity method and the developed three-dimensional (3D) theoretical approach to obtain the thermal diffusivity α and heat transfer coefficient H of air at low pressures in the range from 760 to 2.6 Torr at ambient temperature. A combination of cavity length adjustments and frequency scans at each pressure and the application of the least residual criterion of the Downhill Simplex algorithm is shown to yield optimally accurate values of α and H . The fitting procedure is discussed in detail and the results are compared to previous measurements³ and theoretical data calculated via the thermodynamic equation of state for an ideal gas.

II. EXPERIMENTAL SETUP

The schematic drawing of the thermal-wave cavity is presented in Fig. 1. The brass film converts the modulated optical energy of the collimated laser beam (400 mW, $\lambda = 806$ nm, Coherent Inc.) into thermal waves. The induced temperature fluctuations propagate through the intracavity air by conduction and radiation mechanisms and are detected by the photopyroelectric sensor (PVDF film) at the opposite side.

To evacuate the thermal-wave cavity for performing low pressure experiments, the experimental setup was installed inside a vacuum chamber. The chamber was then connected to a rotary vane vacuum pump (“TRIVAC A” D2A, Leybold-

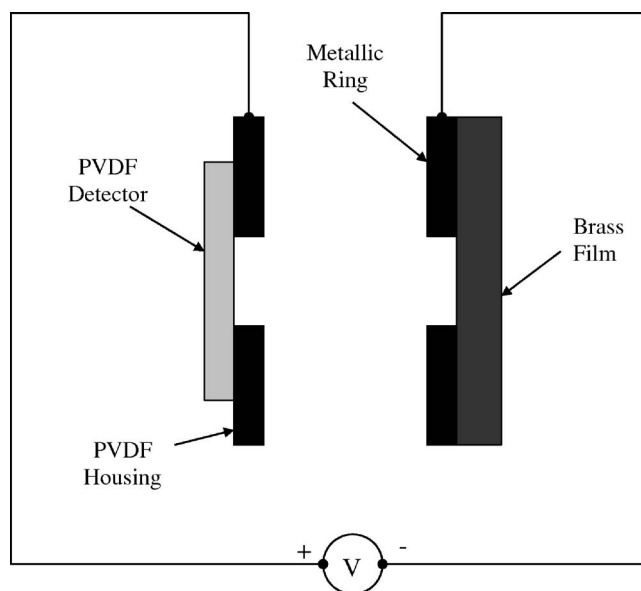


FIG. 2. Schematic of electrical circuit for locating “zero” cavity length.

Heraeus Vacuum Products Inc.) to continuously remove air molecules from the experimental chamber in order to maintain a constant pressure throughout the experiment. All the openings of the vacuum chamber, which allow the wires and the laser fiber-optic cable to pass through, were sealed using vacuum epoxy (“Torr Seal,” Varian Inc.) in order to ensure a sufficiently low experimental pressure. Using the foregoing setup, the lowest operational pressure achieved was 2.6 Torr as indicated by the vacuum gauge (Combitron MC330, Leybold-Heraeus Vacuum Products Inc.).

In order to enhance the accuracy of the experiments, a special electrical circuit was designed to determine the absolute cavity length of the experimental apparatus. The cavity length of the thermal-wave cavity is an important control parameter and the knowledge of it is crucial to the accuracy of the theoretical fits. However, it is extremely difficult to visually determine the “zero position” (the exact position at which the PVDF housing touches the metallic ring that secures the brass film). Consequently, a circuit based on electrical continuity measurements was devised and implemented to locate the zero position. A schematic drawing of this circuit is shown in Fig. 2. Wires were attached separately to the PVDF housing and to the movable part that holds the collimated laser beam. These wires were then connected to a multimeter. The movable laser holder was isolated electrically from all other metallic components of the apparatus to ensure that there is an open circuit unless the PVDF housing contacts it.

Once the PVDF housing makes contact with the laser holder, the circuit is closed as indicated by the multimeter. The cavity length can then be determined accurately by adding the thicknesses of the components that separate the brass film and the PVDF detector. The minimal cavity length (at zero position) is 1.04 mm. The absolute cavity length was henceforth determined by adding 1.04 mm to the distance from the zero position indicated by the micrometer.

The pressure change during the experiments was per-

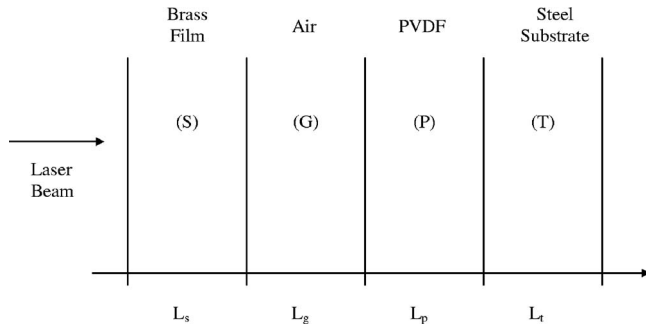


FIG. 3. One-dimensional geometry of the TWC.

formed very gradually in order to ensure uniformity of the pressure distribution over the PVDF film and eliminate pressure effects on the sensor.

III. ONE-DIMENSIONAL TWC THEORY

Figure 3 presents the four layers considered in the formulation of the one-dimensional theory. The brass film (S) converts the modulated optical energy of the collimated laser beam into thermal waves. The induced temperature fluctuations then propagate through the intracavity air (G) by conduction and radiation mechanisms and are detected by the photopyroelectric sensor (P). The steel substrate (T) is considered semi-infinite as its thickness is much greater than the thermal diffusion depth $\lambda_t(\omega) = \sqrt{2\alpha_t/\omega}$ in steel, where α_t is the thermal diffusivity and ω is the modulation angular frequency.

If the spot size of the laser beam is large compared to the thermal diffusion length of the intracavity gas $\lambda_g(\omega) = \sqrt{2\alpha_g/\omega}$, the thermal-wave field can be considered one dimensional and the temperature field inside every element of the cavity may be described by the one-dimensional heat conduction equation,

$$\frac{d^2}{dx^2}T(x, \omega) - \sigma^2 T(x, \omega) = -\frac{1}{k}Q(x, \omega), \quad (1)$$

$$\sigma = (1 + i)\sqrt{\omega/2\alpha}. \quad (2)$$

The parameter σ has units of m^{-1} and has the physical meaning of a complex thermal diffusion coefficient. k is the thermal conductivity of the medium and $Q(x, \omega)$ is the thermal-wave source term.

With the absence of an internal heat source in each of the layers, the heat conduction equation for the four layers can be simplified as follows:

$$\frac{d^2}{dx^2}T_i(x, \omega) - \sigma_i^2 T_i(x, \omega) = 0, \quad (3)$$

where the subscript i refers to the i th layer in the experimental geometry, i being S, G, P, or T (Fig. 3).

Experimental results indicate that radiation becomes a prominent contributor to the PVDF signal under room pressure at higher frequencies when the cavity length is sufficiently large. To account for the effects of radiation, we included the radiation heat flux F_{IR} at the brass film-air boundary,

$$F_{IR} = \sigma_{SB}\epsilon_s T_s^4(L_s, \omega) \quad (4)$$

where $\sigma_{SB} = 5.67 \times 10^{-8} \text{ W m}^{-2} \text{ K}^{-4}$ is the Stefan-Boltzmann constant and $0 \leq \epsilon_s \leq 1$ is the spectrally averaged infrared emissivity of brass. T_s is the temperature of the brass film at the boundary L_s , which includes a small oscillating component at angular frequency ω . The ac component of infrared flux can be linearized as follows:²⁵

$$F_{IR} \approx 4\sigma_{SB}\epsilon_s T_{sdc}^3 T_{sac} \equiv HT_{sac} \quad (5)$$

where $T_s = T_{sdc} + T_{sac}$. From this point on, we consider only ac temperature and flux, therefore we omit the *ac* subscript.

The boundary conditions across and at the exterior boundaries of the four layers S, G, P, and T presented in Fig. 3 can be written as

$$(a) -k_s \left. \frac{dT_s}{dx} \right|_{x=0} = \frac{I_0}{2},$$

$$(b) T_s(L_s) = T_g(L_s),$$

$$(c) k_s \left. \frac{dT_s}{dx} \right|_{x=L_s} = k_g \left. \frac{dT_g}{dx} \right|_{x=L_s} - HT_s(L_s),$$

$$(d) T_g(L_s + L_g) = T_p(L_s + L_g),$$

$$(e) k_g \left. \frac{dT_g}{dx} \right|_{x=L_s+L_g} = k_p \left. \frac{dT_p}{dx} \right|_{x=L_s+L_g} + HT_s(L_s + L_g),$$

$$(f) T_p(L_s + L_g + L_p) = T_t(L_s + L_g + L_p),$$

$$(g) k_p \left. \frac{dT_p}{dx} \right|_{x=L_s+L_g+L_p} = k_t \left. \frac{dT_t}{dx} \right|_{x=L_s+L_g+L_p},$$

$$(h) k_t \left. \frac{dT_t}{dx} \right|_{x=L_s+L_g+L_p+L_t} = 0. \quad (6)$$

Here, I_0 is the intensity of the laser beam, assumed spatially uniform.

Solving the boundary-value problem with the system of four equations [Eq. (3)] in regions S, G, P, and T and the boundary conditions [Eq. (6)] gives the expression for the PVDF temperature $T_p(x, \omega)$. The thermal-wave signal can then be related to the PVDF output voltage by the following integral:

$$V(\omega) = S(\omega) \frac{1}{L_p} \int_{L_p} T_p(x, \omega) dx, \quad (7)$$

where $S(\omega)$ is the instrumental transfer function. After performing the above integration, the expression for the PVDF voltage signal is²⁵

$$V(\omega) = \frac{S(\omega)(2I_0/k_g\sigma_g\sigma_p)(1 - e^{-L_p\sigma_p})(Y_{ip} + X_{ip}e^{-L_p\sigma_p}) \left[(1 - e^{-2L_g\sigma_g}) \frac{H}{k_p\sigma_p} + 2b_{gp}e^{-L_g\sigma_g} \right]}{(1 - e^{-2L_s\sigma_s})(H/k_g\sigma_g)\{(1 - e^{-2L_g\sigma_g})Q_{ip} + P_{ip}[(1 + e^{-2L_g\sigma_g})b_{gp} - 2e^{-2L_g\sigma_g}]\} + b_{gp}P_{ip}Q_{sg} + Q_{ip}P_{sg}}, \quad (8a)$$

where $\sigma_j = (1 + i)\sqrt{\omega/2\alpha_j}$,

$$b_{ij} = \frac{k_i\sigma_i}{k_j\sigma_j},$$

$$X_{ij} = (1 - b_{ij}) + (1 + b_{ij})e^{-2L_i\sigma_i}, \quad (8b)$$

$$Y_{ij} = (1 + b_{ij}) + (1 - b_{ij})e^{-2L_i\sigma_i},$$

$$P_{ij} = (Y_{ij} + X_{ij}e^{-2L_j\sigma_j}),$$

$$Q_{ij} = (Y_{ij} - X_{ij}e^{-2L_j\sigma_j}).$$

The experimental transfer function $S(\omega)$ was normalized out by taking the ratio of the cavity signal to the photopyroelectric signal produced by direct laser light incident on the PVDF sensor.²⁵

$$T_{3D}(x; \omega) = \frac{4W}{a^2} \int_0^\infty T_{1D}(x, s) e^{-(\mu/2)^2} \left[\int_0^a J_0(\mu r/W) r dr \right] \mu d\mu = \frac{4W}{a^2} \int_0^\infty T_{1D}(x, s) e^{-(\mu/2)^2} J_1(\mu a/W) \mu d\mu. \quad (10)$$

Here, a is the effective detector size and J_1 is the Bessel function of the first kind of order 1. Employing the expression of photopyroelectric voltage dependence on the temperature [Eq. (7)], the 3D signal takes the final form

$$V_{3D}(\omega) = S(\omega) \frac{4W}{a^2} \int_0^\infty V_{1D}[s(\omega, \mu)] e^{-(\mu/2)^2} J_1(\mu a/W) \mu d\mu. \quad (11)$$

V. RESULTS AND DISCUSSION

Examples of the experimental results of frequency scans are presented in Fig. 4 (760 Torr—highest pressure), Fig. 5 (10 Torr—low pressure), and Fig. 6 (2.6 Torr—lowest measured pressure). Here, the continuous lines correspond to the best fits to the 3D model Eq. (11). The parameters of the setup used in the fitting algorithm are presented in Table I. The relative humidity of air during the experiments was approximately 43%. One of the important fitting parameter is the thermal conductivity of air. At low pressures, thermal conductivity data can rarely be found in literature. The existing studies contain the data for temperatures of 0 and 100 °C only.^{21–24} The experimental data of those authors show slight decrease of thermal conductivity at the pressure range of up

IV. THREE-DIMENSIONAL MODEL

The three-dimensional thermal-wave field in a cylindrical domain of infinite lateral dimensions, which is generated by a Gaussian laser source, is given by the calculation of a Hankel integral through the transformation of the thermal-wave vector from $\sigma(\omega)$ to $s(\omega, \mu) = \sqrt{\sigma^2 + (\mu/W)^2}$ as follows:²⁰

$$T_{3D}(r, x; \omega) = 2W \int_0^\infty T_{1D}[x, \sigma(\omega)] \rightarrow s(\omega, \mu) e^{-(\mu/2)^2} J_0(\mu r/W) \mu d\mu. \quad (9)$$

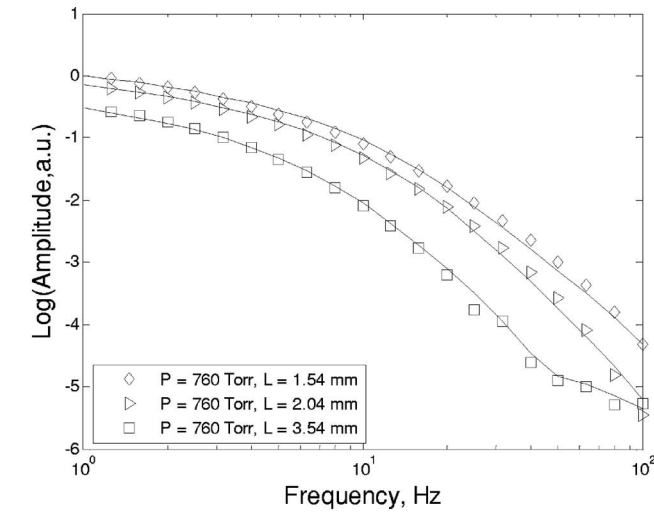
Here, W is the spot size (effective radius) of the laser beam and J_0 is the Bessel function of the first kind of order zero. $T_{1D}(x, \omega)$ is the one-dimensional (1D) thermal-wave field $T_p(x, \omega)$, as calculated in Eq. (7).

To take into account the finite dimensions of the PVDF detector, the signal is integrated and averaged over the size of the detector and becomes

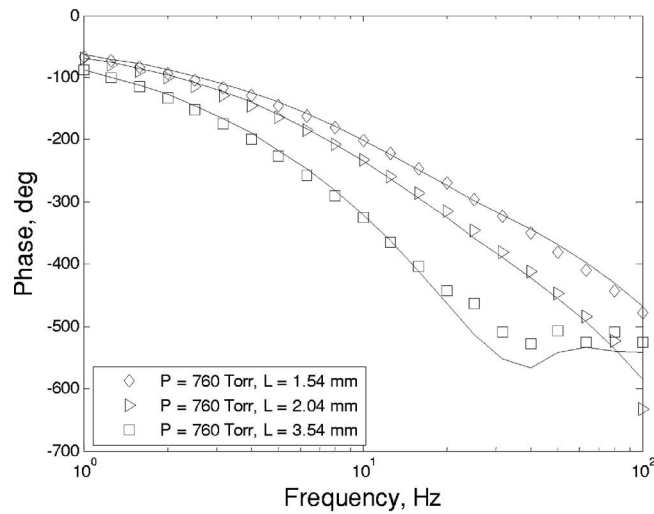
to about 50 Torr, which may be explained by the dimensionality of the setup construction. However, the investigated pressure range in our experiments is still far from the ballistic heat transfer, mean-free-path-limited regime for the experimental conditions of our study. Therefore, the ideal gas laws and the diffusion equation are strictly valid for describing the heat transfer mechanisms (conductive and radiative) throughout this study. The smallest cavity length used in the measurements is 1.54 mm, while the mean free path in air at the lowest pressure (2.6 Torr) is about 10 μm (at 760 Torr, it is 0.1 μm).²⁸ Based on this fact, we set the thermal conductivity to be a constant value, $\kappa = 0.026 \text{ W m}^{-1} \text{ K}^{-1}$, for the investigated pressure range.²⁹

In the fitting process, all the parameters were kept fixed except the thermal diffusivity value. The procedure of finding the best thermal diffusivity included several steps. First, the thermal diffusivity of air at every pressure was fitted to the measurement data at every cavity length. The fitting was repeated for the series of the heat transfer coefficients [Eq. (5)], which were varied from 0 to 1 (Fig. 7).

The pair of the fitted α and H values with the least residual error between theoretical and experimental signal was accepted as the best fitted parameters. Figure 7(b) shows

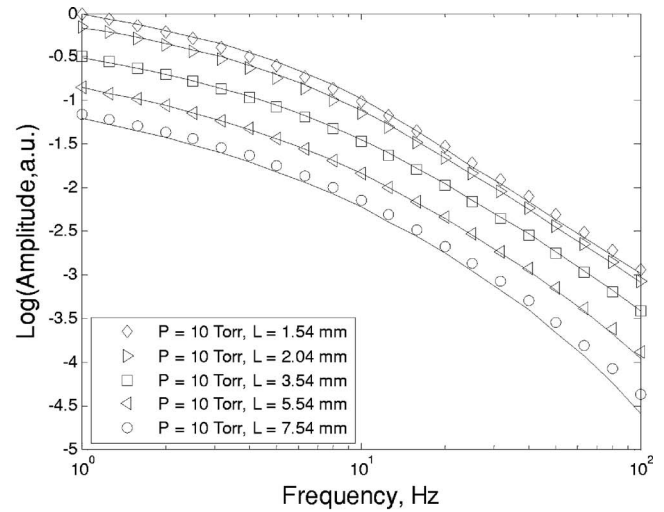


(a)

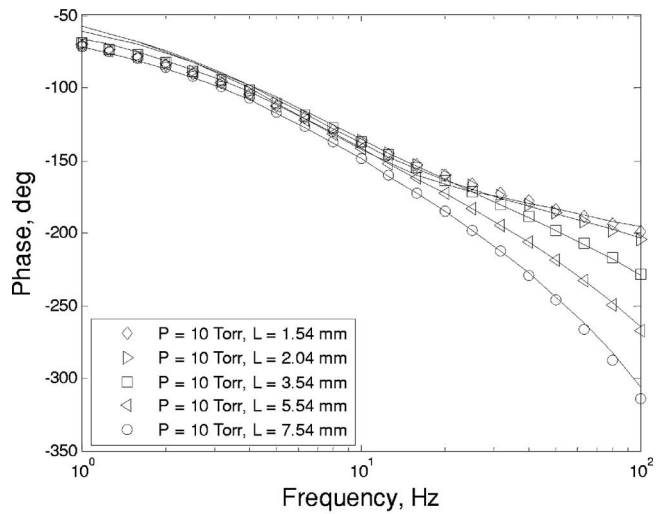


(b)

FIG. 4. Frequency scans at 760 Torr: (a) amplitude and (b) phase.



(a)



(b)

FIG. 5. Frequency scans at 10 Torr: (a) amplitude and (b) phase.

that, for smaller cavity lengths ($L=1-3$ mm), there is a very slight residual dependence on H . That means that the optimal value of H is not well defined in this region of L . Therefore, larger cavity lengths are preferred for the H evaluation.

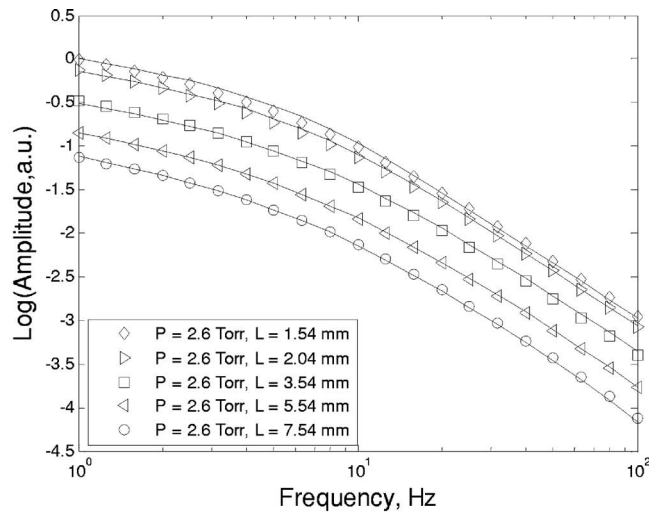
The residual used for the fits was defined as

$$Res = \frac{\sum_{n=1}^{n_{max}} [\log_{10}(Amp_{Exp}) - \log_{10}(Amp_{Theor})]^2}{\sum_{n=1}^{n_{max}} [\log_{10}(Amp_{Exp})]^2} + \frac{\sum_{n=1}^{n_{max}} [Phase_{Exp} - Phase_{Theor}]^2}{\sum_{n=1}^{n_{max}} [Phase_{Exp}]^2}, \quad (12)$$

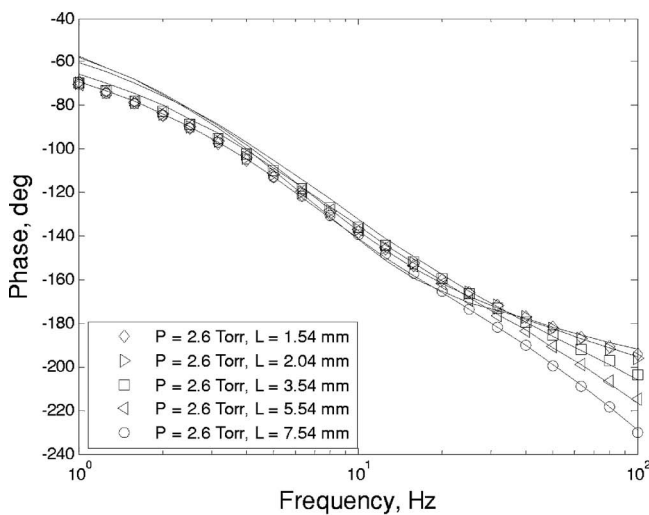
where Amp_{Exp} and $Phase_{Exp}$ are the measured amplitude and phase, Amp_{Theor} and $Phase_{Theor}$ are calculated data, n_{max} is a number of frequency-scan points. Here, the overall residual error includes information on both amplitude and phase channels of the output signal. Due to the large change in

amplitude during experiments, the amplitude values were analyzed on a logarithmic scale. In the search for minimal residual, the Downhill Simplex minimization algorithm was utilized.³⁰ Although this algorithm allows finding the minimum of a function of more than one independent variable, the attempt to use two-parameter (α, H) fits resulted sometimes in negative best fits of H , especially for the small cavity lengths where the residual dependence on H is not well-defined [Fig. 7(b)]. Negative values of heat transfer coefficient [Eq. (5)] have no physical meaning. Therefore, we fitted thermal diffusivity α only for a set of fixed positive values of H , and then chose the pair of (α, H) with the lowest residual [Eq. (11)], as described above.

The minimal residual for all pressures is shown in Fig. 8 as a function of the cavity length. Except for the pressure $P=760$ Torr, minimal residuals mostly occur at $L=5.5-7.5$ mm. The residual increases for the larger cavity lengths, which can be explained by the fact that the detected thermal-wave transmission signal becomes weaker at larger distances, which can lead to higher measurement uncertainty. This effect is more pronounced at ambient pressure, $P=760$ Torr, since the thermal diffusivity here is lowest and,



(a)



(b)

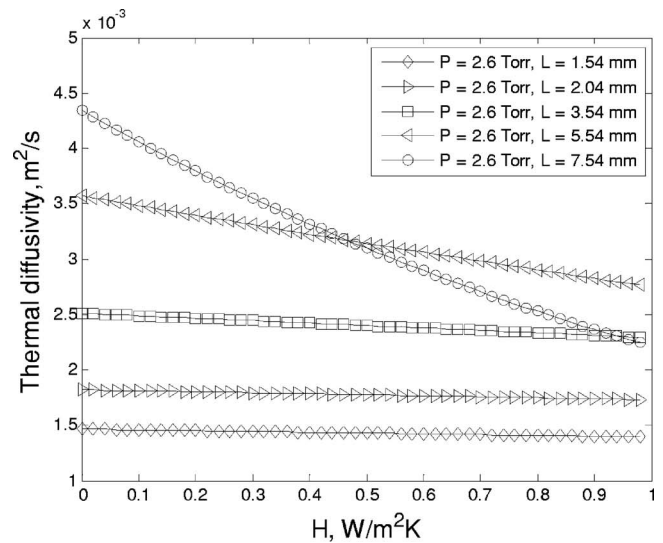
FIG. 6. Frequency scans at 2.6 Torr: (a) amplitude and (b) phase.

consequently, the thermal diffusion length $\lambda_g(\omega)$ is much smaller than at low pressures. Therefore, the transmitted thermal-wave amplitude is smaller, which results in considerably lower TWC signal strength.

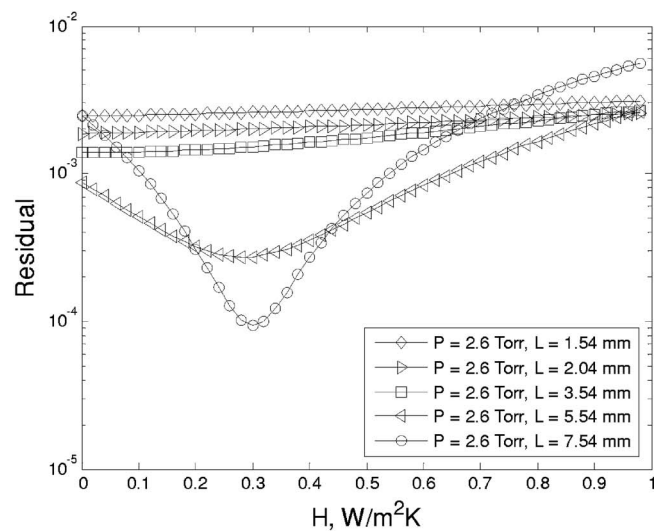
The smaller cavity lengths at low pressures lead to increase in residual as well (Fig. 8), due to inaccuracy in the detection of the transmitted energy. Indeed, at higher thermal diffusivity values, thermal diffusion length increases, thus strengthening the transmitted flux in all directions. At the same time, the size of the PVDF detector remains the same throughout the entire series of the experiments. Therefore, at

TABLE I. Parameters of materials used in fitting algorithm.

	Thermal diffusivity α ($\text{m}^2 \text{s}^{-1}$)	Thermal conductivity k ($\text{W m}^{-1} \text{K}^{-1}$)	Thickness L (m)
Brass film ^a	3.412×10^{-5}	111	35×10^{-6}
PVDF film ^b	7.6×10^{-8}	0.19	52×10^{-6}
Aluminum substrate ^a	9.7×10^{-6}	36	1.5×10^{-3}

^aReference 26.^bReference 27.

(a)



(b)

FIG. 7. Illustration of the fitting process for $P=2.6$ Torr: (a) best fitted thermal diffusivity at various values of H and cavity lengths and (b) corresponding residual of the fittings.

low pressures, the rms radius of the thermal-wave field becomes larger than the radius of the detector, so the active element captures a smaller solid angle of the transmitted thermal-wave flux. This leads to partly unaccounted losses of detected thermal-wave flux and increases the residual of the fittings.

The values of the fitted thermal diffusivity, found according to the minimal residual search, and the corresponding heat transfer coefficients are presented in Fig. 9 as a function of the cavity length. Although the fitted thermal diffusivity should not depend on the cavity length, at the smaller cavity lengths the values exhibit a slight dependence, especially at low pressures, which, again, can be explained by the aforementioned reasons.

As a result of the analysis of the measured data, the optimal cavity length for most reliable measurements at low pressures, according to the described best-fit criteria, was chosen to be $L=7.54$ mm at $P=2.6$ Torr and $P=4$ Torr; $L=5.54$ mm at $P=6$ Torr and $P=10$ Torr; $L=1.54$ mm at

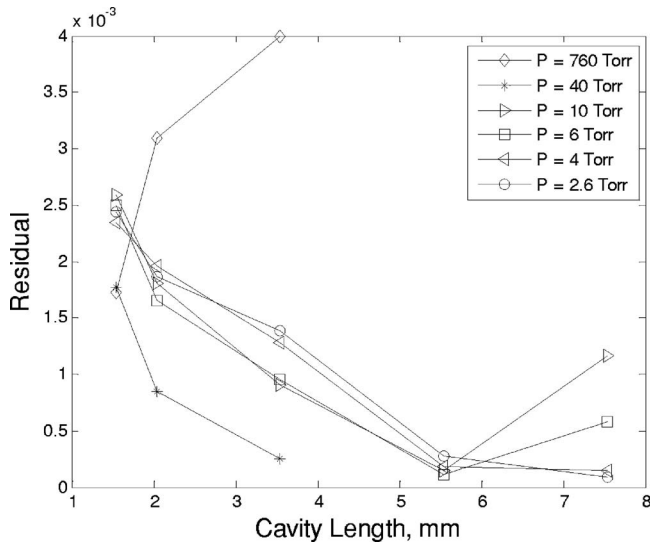
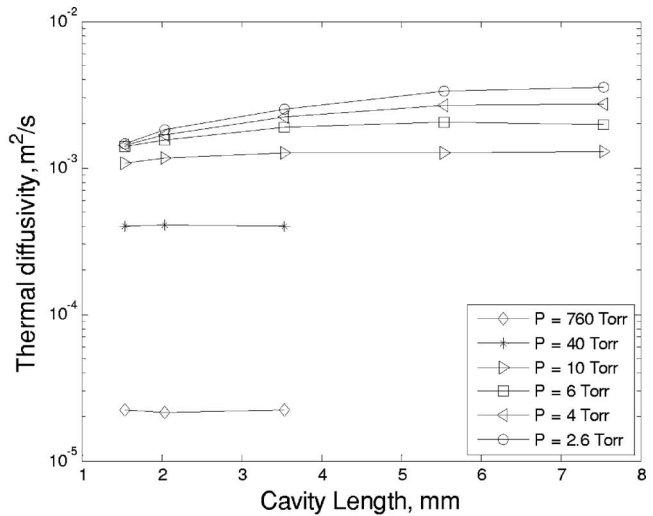


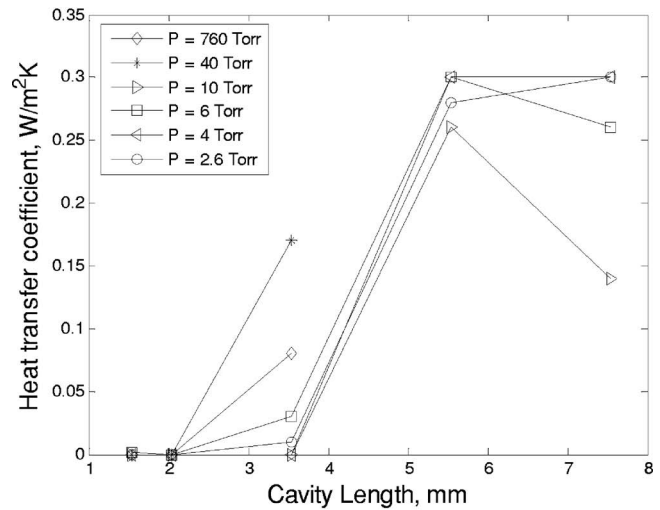
FIG. 8. Calculated minimal residual vs cavity length.

room pressure; and at $P=40$ Torr, $L=3.54$ mm (there were no data for $L=5.54$ mm at this particular pressure). The thermal diffusivity values fitted at these values of L and the corresponding heat transfer coefficients which provided the minimal residual were accepted as the best fitted parameters (Table II) and used to plot the theoretical curves for various pressures, Fig. 10. The analysis of the shape of the curves shows that, for low pressure regimes, there is no significant influence of the radiative component. Indeed, the thermal diffusivity of air increases dramatically at low pressures,³ so the radiation flux, mostly independent of pressure, becomes negligible in comparison to the conduction flux. At a small cavity length ($L=1.54$ mm), the room pressure curve also did not show the influence of the radiative component (Fig. 10). However, at larger cavity lengths, the high-frequency end of the room pressure scan exhibits a “flat” transition area (Fig. 4) associated with decreasing importance of the conduction transport mechanism and increasing dominance of radiation.²⁵ Consequently, the conduction-only version of the model, which can be obtained by setting H in Eq. (8) to zero, is still valid at larger cavities for the low pressure measurements (Fig. 11), but the high-frequency range of the room pressure signal can be adequately described only by applying the radiative component of the theory.

The application of 1D theory [Eq. (8)] to fitting the data does not give good agreement with experiment, especially



(a)



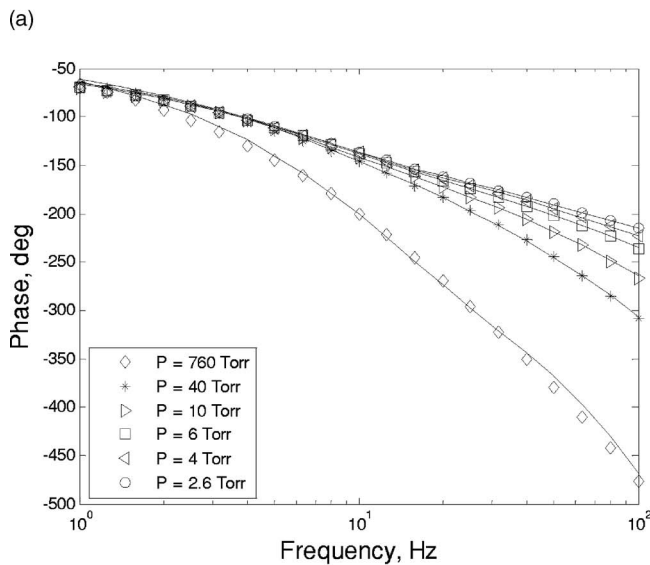
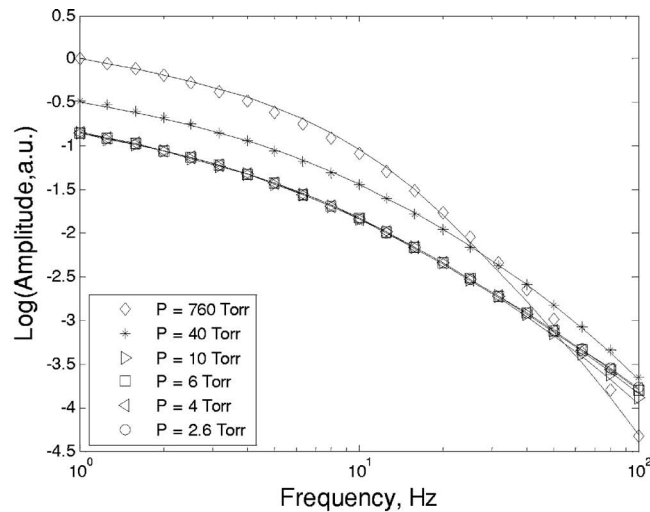
(b)

FIG. 9. Thermal diffusivity (a) and heat transfer coefficient (b) found according to the least residual analysis for various pressures.

the low-frequency phases at low pressures (Fig. 12). The fitting procedure was the same as applied for the 3D analysis. The fitted curves diverge from the experimental points at lower frequencies, where the thermal diffusion lengths $\lambda = \sqrt{2\alpha/\omega}$ are large and the three-dimensionality of the process is more pronounced. The radial expansion of the

TABLE II. Fitting parameters for air. The α and H values are measured at the cavity length of the lowest residual, Figs. 8 and 9.

Pressure P (Torr)	Thermal diffusivity α ($\text{m}^2 \text{s}^{-1}$)	Heat transfer coefficient H ($\text{W m}^{-2} \text{K}^{-1}$)	Specific heat capacity c_p ($\text{J kg}^{-1} \text{K}^{-1}$)	Cavity length L (mm)	Residual R ($\times 10^{-3}$)
760	$(2.2347 \pm 0.0013) \cdot 10^{-5}$	0.000 ± 0.000	1006.337	1.54	1.727 ± 0.015
40	$(4.0106 \pm 0.0041) \cdot 10^{-4}$	0.170 ± 0.002	1004.736	3.54	0.250 ± 0.001
10	$(1.2709 \pm 0.0052) \cdot 10^{-3}$	0.258 ± 0.003	1004.682	5.54	0.145 ± 0.003
6	$(2.0401 \pm 0.0067) \cdot 10^{-3}$	0.299 ± 0.001	1004.675	5.54	0.109 ± 0.003
4	$(2.7227 \pm 0.0190) \cdot 10^{-3}$	0.300 ± 0.003	1004.672	7.54	0.145 ± 0.007
2.6	$(3.5457 \pm 0.0214) \cdot 10^{-3}$	0.302 ± 0.002	1004.669	7.54	0.093 ± 0.003



(b)

FIG. 10. Frequency scans at various pressures: (a) amplitude and (b) phase. Continuous lines correspond to the best fits to the 3D model. The optimal cavity lengths are $L=7.54$ mm at $P=2.6\text{--}4$ Torr, $L=5.54$ mm at $P=6\text{--}10$ Torr, $L=3.54$ mm at $P=40$ Torr, and $L=1.54$ mm at $P=760$ Torr.

thermal-wave field here is significant. Consequently, the field cannot be considered as one-dimensional, and three-dimensional theory is necessary to take into account the radial energy transfer. This effect is less noticeable for ambient room pressure (Fig. 13), where thermal diffusivity is lower and the thermal diffusion length is smaller. However, the divergence between the theory and experiment is noticeable at low frequencies, where the nonlongitudinal flux is significant but not accounted for by the 1D model. In this case, the sideways flux contributes to shifting the thermal-wave centroid closer to the pyroelectric detector, thus decreasing the phase lag and the amplitude compared to purely longitudinal (1D) diffusion. These effects, especially the phase shift, are clearly observed in Figs. 12 and 13.

The best parameter pair (α, H) fitted with the 3D model (Table II) is shown in Fig. 14 as a function of pressure. The error bars correspond to the standard deviation based on the five consecutive measurements of the PVDF signal voltage at exactly the same conditions. The mean of the fitted param-

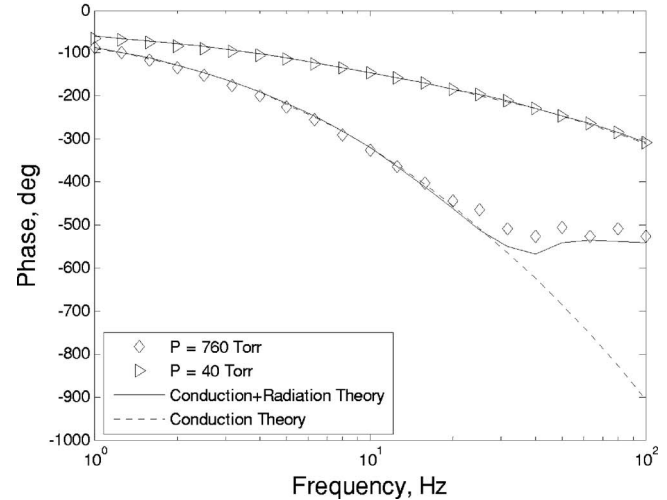
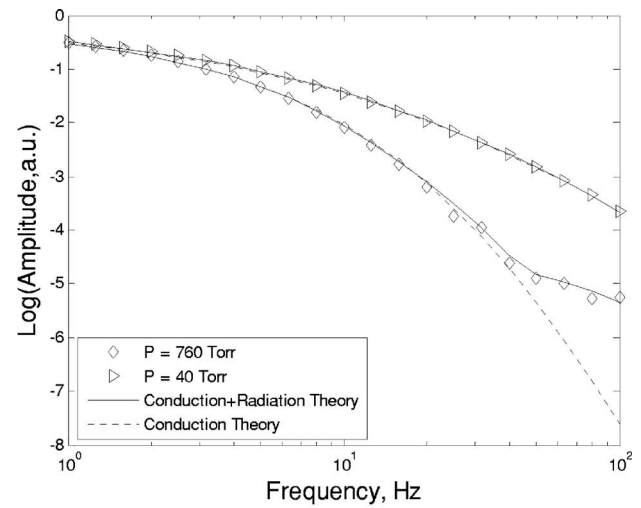


FIG. 11. Conduction vs conduction-radiation theory at ambient and low pressure scans ($L=3.54$ mm).

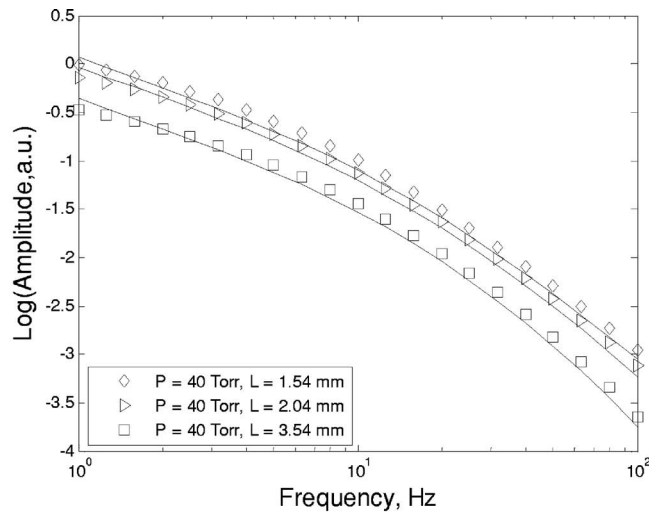
eters corresponds to the fitting of the frequency curve of the mean measured signal, while the standard deviation of the parameters is obtained by the fitting of the mean signal plus/minus standard deviation of the signal. The small values of the error bars demonstrate the stability and robustness of the measurement system. The results of the study are compared to the theoretical values (Fig. 14) calculated using the definition of thermal diffusivity,

$$\alpha = \frac{k}{\rho c_p}. \quad (13)$$

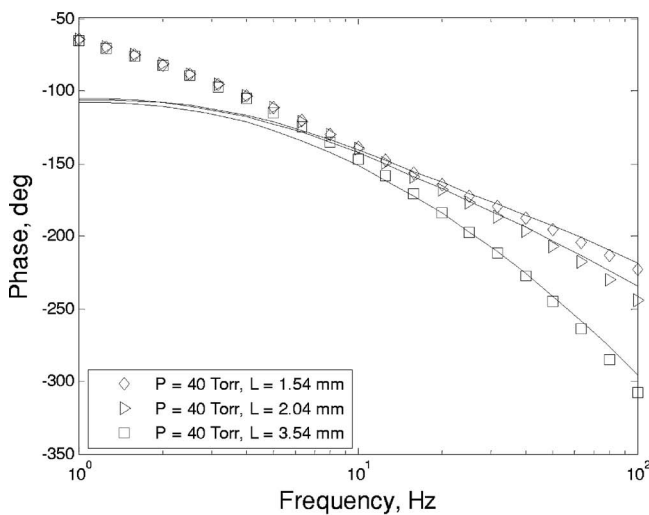
Here, the thermal conductivity $k=0.026$ W m⁻¹ K⁻¹ and the specific heat capacity of air,³¹ c_p , J kg⁻¹ K⁻¹, are shown in Table II. The density of air is calculated according to the thermodynamic equation of state for an ideal gas,³

$$P = \frac{\rho RT}{M}, \quad (14)$$

where $R=8.314$ J mol⁻¹ K⁻¹ is the universal gas constant and $M=28.8 \times 10^{-3}$ kg/mole is the average molar mass of air.³² Also, the results at $P=760$ Torr and $P=40$ Torr are compared to the values of thermal diffusivity measured previously.³ The lowest pressure measured in that study was 40 Torr, in which the authors used similar methodology for



(a)

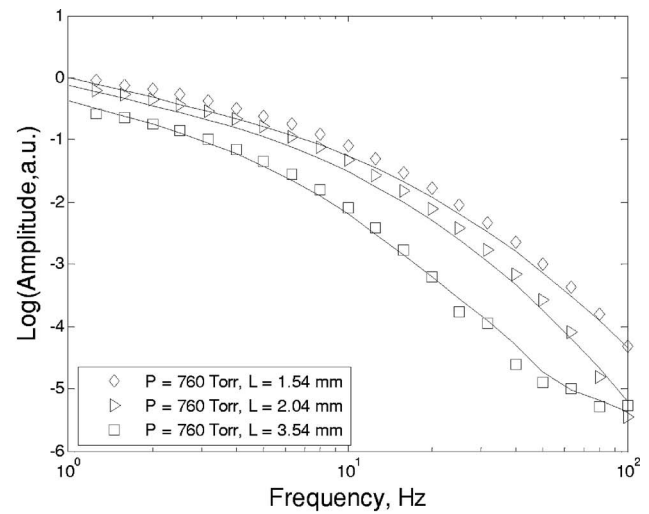


(b)

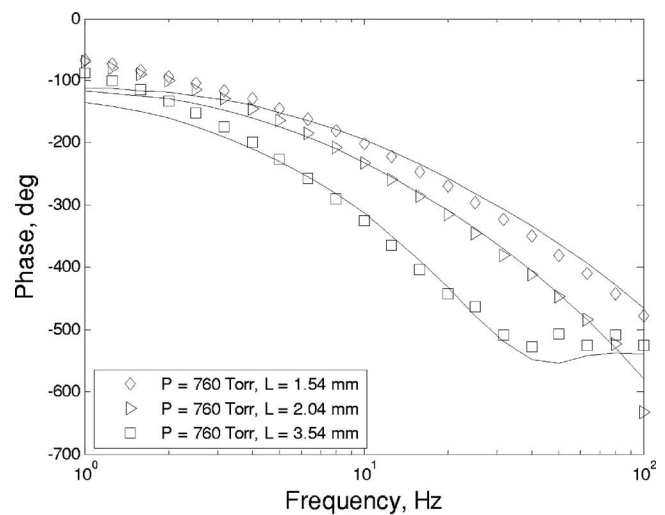
FIG. 12. Frequency scans at 40 Torr: (a) amplitude and (b) phase. Continuous lines correspond to the best fits with the 1D theoretical model, Eq. (8).

the measurements. There was a difference in the measurement cell,³ however. Instead of laser-induced temperature oscillations, a thin-film strip resistive heater was used. In this case, the nonuniformity of the generated thermal-wave field most likely introduced some errors during the measurements. Moreover, the authors used a 1D theoretical approach. The comparison of the results shows that a 3D model combined with an azimuthally symmetric thermal-wave source can substantially improve the results.

The radiative heat transfer coefficient increases with decreasing pressure [Fig. 14(b)]. A tentative interpretation of the dependence on pressure is that the gradual establishment of relative vacuum on the gaseous side of the brass film-air interface impedes the conductive transfer of heat to the gas, thus increasing the interface temperature and the radiation heat transfer coefficient $H=4\sigma_{SB}\epsilon_s T_{dc}^3$ with decreasing pressure. However, the radiation component is still small here compared to the conductive component, since the thermal diffusivity at low pressures increases much faster than the heat transfer coefficient (Fig. 14).



(a)

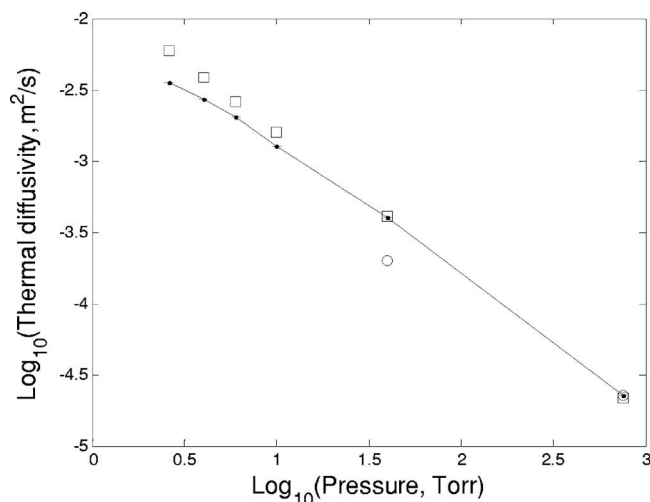


(b)

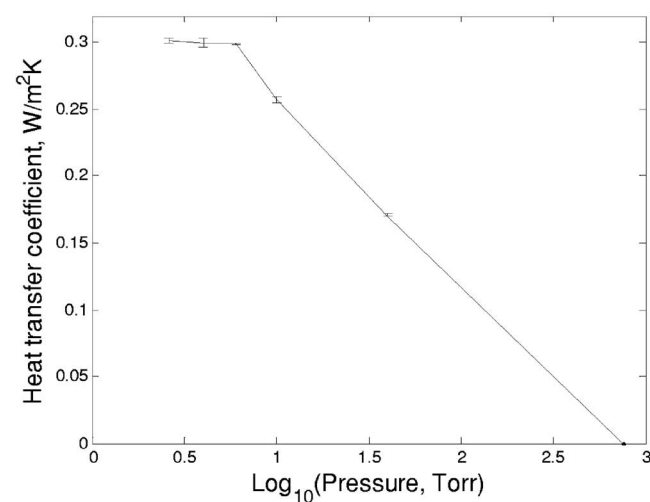
FIG. 13. Frequency scans at 760 Torr: (a) amplitude and (b) phase. Continuous lines correspond to the best fits with the 1D theoretical model, Eq. (8).

Overall, the measurement technique presented in this study allows quantitative thermal characterization of gases at low pressures. With regard to air, thermal diffusivity increases with decreasing pressure, since the density of air decreases significantly with other parameters changing only slightly with pressure drop. Thermal diffusivity values obtained with best fits according to 3D theoretical modeling are in good agreement with the theoretical values calculated from the Eqs. (13) and (14). The heat transfer coefficient at various pressures was also determined simultaneously. In order to achieve the highest possible accuracy of the measurements, adjustment of the cavity length at each particular pressure was involved. At each particular cavity length, values of thermal diffusivity were fitted and the residual of the fitting process was calculated. The cavity length with the lowest residual of the fittings was accepted as a criterion for optimally accurate measurements of α and H .

The presented methodology for the TWC-based measurements at low pressure shows considerable improvement in accuracy compared to the previously published



(a)



(b)

FIG. 14. Best fitted values of (a) thermal diffusivity and (b) heat transfer coefficient as a function of pressure. The continuous curves were obtained by drawing straight lines between experimental points. The thermal diffusivity curve is compared to the calculated theoretical values (squares) and two points obtained in Ref. 3 (circles).

technique.³ The main reasons for that are the application of laser-induced azimuthally symmetric thermal-wave source, the use of a 3D theoretical approach for the calculation of thermal parameters, and the judicious adjustment of cavity length so as to yield maximum sensitivity to both diffusivity and heat transfer coefficient as functions of pressure. Also, the applied frequency-scan method avoids the position (absolute cavity length) measurement uncertainty, which is an inherent disadvantage of the length-scan methods used in the literature.³ In conclusion, the TWC was shown to be an effective and accurate tool for the thermal characterization of air. This study becomes even more important due to the lack of published data on the thermal conductive and radiative properties of air at low pressures.

ACKNOWLEDGMENTS

The support of the National Sciences and Engineering research Council of Canada (NSERC) is gratefully acknowledged. We are grateful to K. Yan, L. L. Yang, A. Dos Santos, and D. Brahaj for their help with this project.

- ¹J. Shen and A. Mandelis, *Rev. Sci. Instrum.* **66**, 4999 (1995).
- ²J. Shen, A. Mandelis, and B. D. Aloysius, *Int. J. Thermophys.* **17**, 1241 (1996).
- ³G. Pan and A. Mandelis, *Rev. Sci. Instrum.* **69**, 2918 (1998).
- ⁴J. A. P. Lima, M. G. da Silva, S. L. Cardoso, and H. Vargas, *Rev. Sci. Instrum.* **74**, 433 (2003).
- ⁵J. Shen, A. Mandelis, and H. Tsai, *Rev. Sci. Instrum.* **69**, 197 (1998).
- ⁶J. A. Balderas-Lopez and A. Mandelis, *Rev. Sci. Instrum.* **72**, 2649 (2001).
- ⁷J. A. Balderas-Lopez and A. Mandelis, *J. Appl. Phys.* **90**, 3296 (2001).
- ⁸J. A. Balderas-Lopez and A. Mandelis, *J. Appl. Phys.* **88**, 6815 (2000).
- ⁹J. A. P. Lima, E. Marin, M. S. O. Massunaga, O. Correa, S. L. Cardoso, H. Vargas, and L. C. M. Miranda, *Appl. Phys. B: Lasers Opt.* **73**, 151 (2001).
- ¹⁰D. Dadarlat, J. Gibkes, D. Bicanic, and A. Pasca, *J. Food. Eng.* **30**, 155 (1996).
- ¹¹D. Dadarlat, H. Vissert, and D. Bicanic, *Meas. Sci. Technol.* **6**, 1215 (1995).
- ¹²N. Morioka, A. Yurai, and T. Nakanishi, *Jpn. J. Appl. Phys., Part 1* **34**, 2579 (1995).
- ¹³J. Caerels, C. Glorieux, and J. Thoen, *Rev. Sci. Instrum.* **69**, 2452 (1998).
- ¹⁴J. Caerels, C. Glorieux, and J. Thoen, *Rev. Sci. Instrum.* **71**, 3506 (2000).
- ¹⁵S. Delenclos, M. Chirtoc, A. H. Sahraoui, C. Kolinsky, and J. M. Buisine, *Rev. Sci. Instrum.* **73**, 2773 (2002).
- ¹⁶D. Dadarlat, C. Neamtu, E. Surducun, A. H. Sahraoui, S. Longuemart, and D. Bicanic, *Instrum. Sci. Technol.* **30**, 387 (2002).
- ¹⁷M. Chirtoc, E. H. Bentefour, C. Glorieux, and J. Thoen, *Thermochim. Acta* **377**, 105 (2001).
- ¹⁸C. Wang and A. Mandelis, *Rev. Sci. Instrum.* **70**, 2372 (1999).
- ¹⁹A. Matvienko and A. Mandelis, *Rev. Sci. Instrum.* **77**, 064906 (2006).
- ²⁰A. Mandelis, *Diffusion-Wave Fields: Mathematical Methods and Green Functions* (Springer, New York, 2001), p. 418.
- ²¹W. G. Kannuluik and E. H. Carman, *Aust. J. Sci. Res., Ser. A* **4**, 305 (1951).
- ²²W. G. Kannuluik and H. B. Donald, *Aust. J. Sci. Res., Ser. A* **3**, 417 (1950).
- ²³W. G. Kannuluik and L. H. Martin, *Proc. R. Soc. London, Ser. A* **144**, 496 (1934).
- ²⁴W. J. Taylor and H. L. Johnston, *J. Chem. Phys.* **14**, 219 (1946).
- ²⁵A. Matvienko and A. Mandelis, *Int. J. Thermophys.* **26**, 837 (2005).
- ²⁶E. R. G. Eckert and R. M. Drake, *Heat and Mass Transfer* (McGraw-Hill, New York, 1959).
- ²⁷Kynar Piezo Film, technical manual, Pennwalt Corp, Valley Forge.
- ²⁸H. U. Poll, U. Schlauditz, and S. Schreiter, *Surf. Coat. Technol.* **142-144**, 489 (2001).
- ²⁹A. A. Vasserman, Ya. Z. Kazavchinskii, and V. A. Rabinovich, *Thermophysical Properties of Air and Air Components* (Israel Program for Scientific Translations Ltd., Jerusalem, 1971).
- ³⁰W. H. Press, S. A. Teukolsky, W. T. Vetterling, and B. P. Flannery, *Numerical Recipes in Fortran*, 2nd ed. (Cambridge University Press, New York, 1992), Vol. 1, Chap. 10.4.
- ³¹J. Hilsenrath, C. W. Beckett, W. S. Benedict, L. Fano, H. J. Hoge, J. F. Masi, R. L. Nuttall, Y. S. Touloukian, and H. W. Woolley, *Tables of Thermal Properties of Gases* (National Bureau of Standards, Washington, D.C., 1955).
- ³²D. Halliday and R. Resnick, *Fundamentals of Physics*, 2nd ed. (Wiley, New York, 1981), Chap. 21.